nature nanotechnology

SUPPLEMENTARY INFORMATION

DOI: 10.1038/NNANO.2011.24

A high-throughput label-free nanoparticle analyzer
Supplementary Information

Jean-Luc Fraikin,[1] Tambet Teesalu,[2] Christopher M. McKenney,[1]
Erkki Ruoslahti,[2,3] Andrew N. Cleland[1*]

[1]Department of Physics, University of California
Santa Barbara, CA 93106, USA
[2]Vascular Mapping Laboratory, Center for Nanomedicine,
Sanford-Burnham Medical Research Institute at University of California
Santa Barbara, CA 93106-9610, USA
[3]Cancer Research Center, Sanford-Burnham Medical Research Institute
La Jolla, CA 92037

DOI: 10.1038/NNANO.2011.24

Supplementary Notes

1 Fabrication

The micromold used to define the microfluidic structure was fabricated using a combination of metal and epoxy features patterned by optical and electron-beam lithography. The substrate consisted of a bare silicon wafer patterned with gold alignment marks. Electron-beam lithography and a standard liftoff process were used to define the gold metal layer for the thin regions of the mold (200-500 nm in thickness), including the fluid resistor and nanoconstriction. The remaining, thicker portions of the microfluidic channel were made of photodefinable epoxy SU-8 (MicroChem Corp., Newton, MA), which was patterned by optical lithography. The mold can be reused indefinitely without apparent degradation. The gold sensing electrode, a few millimeters in length and 200 μm in width, was fabricated on a Pyrex glass substrate using optical lithography and a standard lift-off process. The electrode was 50 nm thick gold with a 10 nm titanium adhesion layer.

2 PDMS molding and final device assembly

The PDMS (10 parts resin:1 part curing agent) was degassed for 2 hours, poured over the mold and cured at 100°C for 40 min. Ports 1 mm in diameter were punched in the PDMS for fluid access (Acupunch, Acuderm Inc., FT Lauderdale, FL), and the PDMS cleaned by sonication in acetone and isopropanol for 3 minutes each. The contact surface of the PDMS was treated for 5 min. in an O_2 plasma immediately prior to bonding. The contact surfaces of the patterned Pyrex chips were prepared for bonding to PDMS with the following steps: Sonication in acetone and isopropanol for 3 minutes each; piranha acid (1 part 30% hydrogen peroxide:3 parts bottle-strength sulfuric acid) for 5 min. at 80°C; rinse in distilled water. The microchannel and electrode were aligned and bonded using a contact aligner (Suss MicroTec), and baked on a hotplate for 15 minutes at 115°C. Short segments of metal tubing were inserted into the PDMS at ports P_1 and P_5, and served as fluidic inlets as well as bias electrodes L and H. Electrical contacts to the sensing electrode were made using 25 μm diameter gold wire bonds.

3 Measurement of the device impedances

The complex electrical impedances of the fluid paths between electrode pairs SH and SL were measured using an *in situ* voltage divider (Supplementary Figure 4). A harmonic voltage of rms amplitude $V_{\mathrm{ac}} = 20$ mV and variable frequency was applied to one of the bias electrodes while the other was left open-terminated. The electrical configuration for the measurement of Z_{a} is shown in Supplementary Figure 4b. The amplitude and phase of the voltage across R_{m} was measured at V_{out} using a lock-in amplifier (SRS Scientific), and the impedance Z_{a} between the

driven bias electrode and the sensing electrode calculated as a function of frequency f, using

$$Z_{\rm a} = R_{\rm m} \cdot (V_{\rm ac}/V_{\rm out}(f) - 1). \quad (1)$$

An equivalent expression holds for $Z_{\rm b}$. The measured real and imaginary parts of $Z_{\rm a}$ and $Z_{\rm b}$ for a typical device with nanoconstriction dimensions $L \times w \times t = 250$ nm $\times$ 250 nm $\times$ 290 nm are shown in Supplementary Figure 4. Each impedance is well-approximated as the series combination of a resistor $R_{\rm a}$ or $R_{\rm b}$, and a capacitance $C_{\rm DL}$. With this model and either of the measured impedances, we calculated $C_{\rm DL} \approx 240$ nF using

$$C_{\rm DL} = -1/(2\pi f \Im(Z_{\rm a})), \quad (2)$$

where $\Im(Z_{\rm a})$ is the imaginary part of $Z_{\rm a}$, and f the frequency of the applied voltage. The exposed area of the sensing electrode was $\sim 10^{-3}$ cm^2, yielding a specific capacitance ~ 240 μF/cm^2 for 1 M NaCl. This capacitance lies within 5% of that expected for the electric double layer at this salt concentration [1], and presents a negligible impedance at measurement frequencies greater than a few Hz.

4 Dynamic electrical response

The dynamic electrical response is modeled by the circuit shown in Fig. 1b, in which the resistance $R_{\rm a}$ includes the impedance of the nanoconstriction, and $R_{\rm b}$ that of the fluid resistor. According to this model, the presence of a particle in the nanoconstriction increases the nanoconstriction resistance by $\Delta R_{\rm a}$. The fluidic resistor-divider generates a change in the fluid potential $V^\star$,

$$\Delta V^\star \approx -\frac{\Delta R_{\rm a}}{R_{\rm a}} \cdot \frac{V_{\rm h} - V_{\rm l}}{R_{\rm a} + R_{\rm b}} \cdot \frac{R_{\rm a} R_{\rm b}}{R_{\rm a} + R_{\rm b}}. \quad (3)$$

The fractional resistance change $\Delta R_{\rm a}/R_{\rm a}$ is proportional to the nanoconstriction filling fraction $f \equiv v_{\rm p}/v_{\rm c}$ for $f \ll 1$, where $v_{\rm p}$ and $v_{\rm c}$ are the volumes of the particle and the nanoconstriction respectively [5]. The voltage change in the fluid is communicated through the relatively large double-layer capacitance of the sensor electrode, which presents a negligible series impedance, so very close to the same voltage change $\Delta V_{\rm out}$ appears on the sensor electrode.

5 Measurement bandwidth

The fluidic voltage-divider implemented here affords a larger detection bandwidth than earlier nanoparticle resistive pulse sensors. These had either employed a source of constant current to bias the nanopore [2], or more commonly, required the sensitive measurement of small currents flowing through the nanopore [3, 4]. These techniques are limited in bandwidth by the current sourcing, or current sensing electronics: In the former case, the large resistance of the

DOI: 10.1038/NNANO.2011.24

nanopore necessitates an even larger output impedance for the current source, which is readily shunted at moderate frequencies by even a minimal stray capacitance; and in the latter, the small current to be measured typically requires a large resistance in the feedback circuit of the current- sensing amplifier, which is likewise readily shunted. By contrast, in our approach the large nanoconstriction resistance is easily biased at constant voltage using a source with a small output impedance. This bias method does not suffer from loss of bandwidth through stray capacitance because of the small output impedance of the source. We maintain the large bandwidth afforded by the resistor-divider by placing a low-noise, low input-capacitance amplifier close to the sensing electrode (a few mm distance), minimizing the stray capacitance in the measurement circuit.

6 Effect of ionic strength on bandwidth and electrical noise

Assuming a balanced resistor divider with $R_{\mathrm{m}} \gg R_{\mathrm{a}} = R_{\mathrm{b}}$, and a linear dependence of fluid conductance on ionic strength, the measurement bandwidth scales linearly with the ionic strength of the analyte suspension Λ, and the thermal Nyquist noise with $\Lambda^{1/2}$. For the plasma experiments we present here, in comparison to measurements in PBS, we expect a slightly slower response time with $f_{\mathrm{RC}} \approx 460$ kHz, and an increase in Nyquist noise of $\sim$18%. Despite the reduction, this bandwidth remains $\sim 100\times$ greater than previous nanoparticle resistive pulse sensors.

7 Flow rate calculation

Finite element software (Comsol Inc, Burlington, MA) was used to model the electric field in the fluid surrounding the nanoconstriction (Supplementary Figure 7). The region of high current density was found to extend from the nanoconstriction into the fluid on either side, with a total length of $L^{\star} \sim 540$ nm (for a nanonconstriction of physical length 250 nm). Since a particle passing through the restriction blocks significant current (thus creating a change in V_{out}) for the duration of time that it is in this volume of high current-density, a volume of fluid $v_{\mathrm{c}}^{\star} = A \times L^{\star}$, where A is the cross sectional area of the nanoconstriction, was assumed to flow through the constriction in the particle transit time. The fluid volume flow rate R was then calculated using,

$$R = \frac{2}{3}\frac{v_{\mathrm{c}}^{\star}}{\tau_{\mathrm{p},117}},$$

where the factor of 2/3 accounts for parabolic laminar flow through the nanoconstriction, and $\tau_{\mathrm{p},117}$ is the mean transit time (full width at half maximum) of 117 nm particles through the nanoconstriction. In the mixture of particles sampled in Figure 3, we found no dependence of mean transit time on particle type (Supplementary Figure 8).

8 Peak analysis

The raw data was first high-pass filtered (typical cutoff frequency ∼100 Hz) to minimize any low frequency undulations in the baseline. These undulations were usually of minimal amplitude, and the filtering had no visible effect on the shapes of the peaks, whose frequency components typically fell in bands higher than ∼1 kHz. When necessary, the data was low-pass filtered using the lowest cutoff frequency that maintained the peak amplitude and shape to within a few percent. All local voltage minima exceeding a particular threshold were considered to be signal events, and each event was then measured individually. A window of width approximately twice the peak width and centered on the minimum was analyzed (Supplementary Figure 5). A local baseline value for each peak was measured by taking the mean value of the outer two quarters of the window (shaded in the figure).

The amplitude of the peak was measured relative to the local baseline, and the uncertainty in this measurement was calculated according to standard error analysis to be:

$$\sigma = \sigma_{\mathrm{b}}\sqrt{1 + 1/N^2}, \tag{4}$$

where the uncertainty in the peak voltage measurement was assumed to equal that in each point of the local baseline σ_{b}, and N was the number of points in the local baseline. The assumption that the baseline and peak uncertainties are equal was justified because the absolute change in R_{a} due to the passage of a particle was too small to change the electrical noise significantly. Peak widths were measured at half-maximum relative to the local base line as indicated by the vertical red lines in the figure.

9 Precision of the technique

A monodisperse population of 117 nm particles was analyzed, and a representative time trace of V_{out} is shown in Supplementary Figure 6a. The peak heights in this trace were measured and the resulting distribution of relative diameters, scaled by the nominal particle diameter, is shown in Supplementary Figure 6b. Two uncertainties contribute to the variance of this distribution: The variance in the actual diameters of the particle population, in addition to any variations arising from the measurement itself (such as noise in the detection voltage). We found the distribution of diameters measured in our detector had a variance (3.3% of the mean) that was less than the variance in particle size (3.9%) specified by the manufacturer. This suggests that our measurement technique has greater precision than the precision of the manufacturer's diametric measurement (disk centrifugation).

10 Distinguishing phage dimers

There are two explanations that justify our identification of particles with an effective 81 nm dia. (Fig. 5b) as agglomerated pairs of phage virions (dimers) rather than the random coincidence

DOI: 10.1038/NNANO.2011.24

of two particles passing simultaneously through the nanoconstriction. First, the concentration of phage in the measured sample was >1000-fold below that for which the average solution volume per particle equals the sensing volume. At this concentration, the probability that two virions occupy the same nanoconstriction volume is thus far below the ~10% population observed in the sample. Second, the distribution of particle transit times for the 65 nm and 81 nm populations do not differ significantly (Supplementary Figure 9). A broader distribution extending to longer transit times would have been expected if the 81 nm signals had been caused by random coincidences.

Supplementary Figures

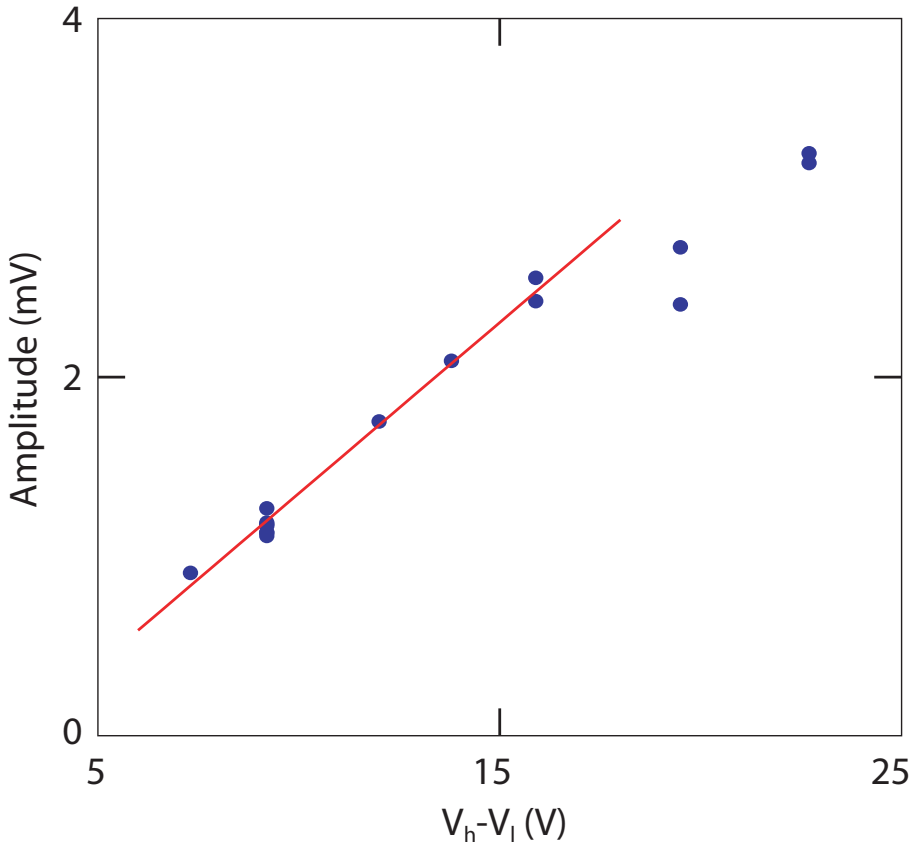

Supplementary Figure 1: The dependence of signal amplitude on bias voltage was linear as expected from Eq. (3), for bias voltages below $V_{\rm h} - V_{\rm l} \sim$18 V. Above this voltage we expect dielectric breakdown of the PDMS that forms the nanoconstriction (Dow Corning literature).

DOI: 10.1038/NNANO.2011.24

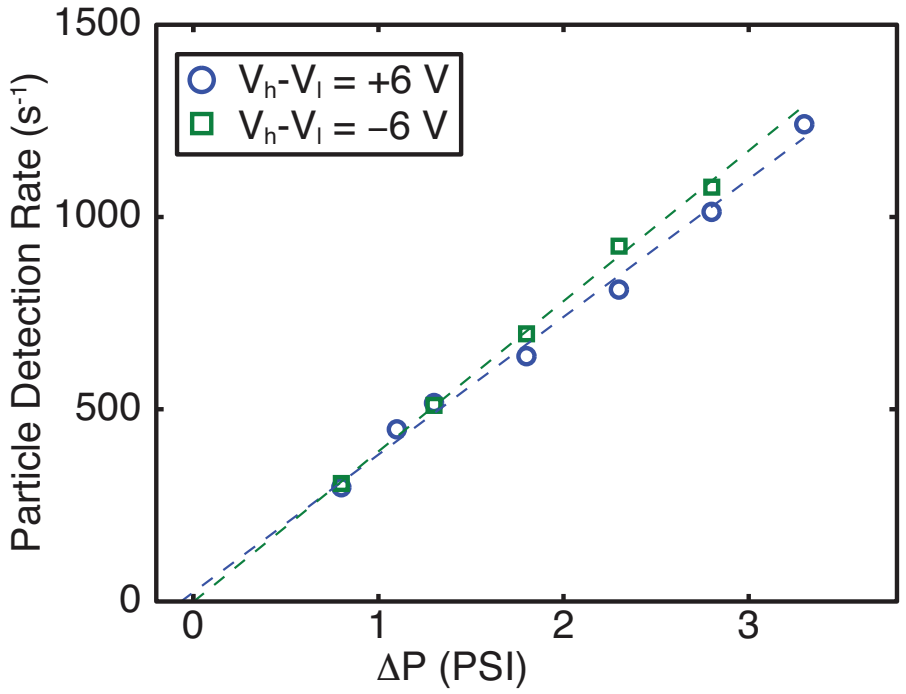

Supplementary Figure 2: Effect of applied pressure and voltage bias on the rate of detection of 117 nm particles. The flow rate of 117 nm particles through the nanoconstriction *vs* approximate pressure drop across the nanoconstriction ΔP, for two voltage bias settings of opposite polarity. ΔP is the measured pressure difference between ports 4 and 5, with an added offset of approximately 0.3 psi to account for the pressure applied at port 6 (see Figure 1a for port numbering). Dashed lines are separate linear fits for each voltage bias, and each passes through the origin within the measurement error. From this data we conclude that electrokinetic and electroosmotic effects are negligible in the system.

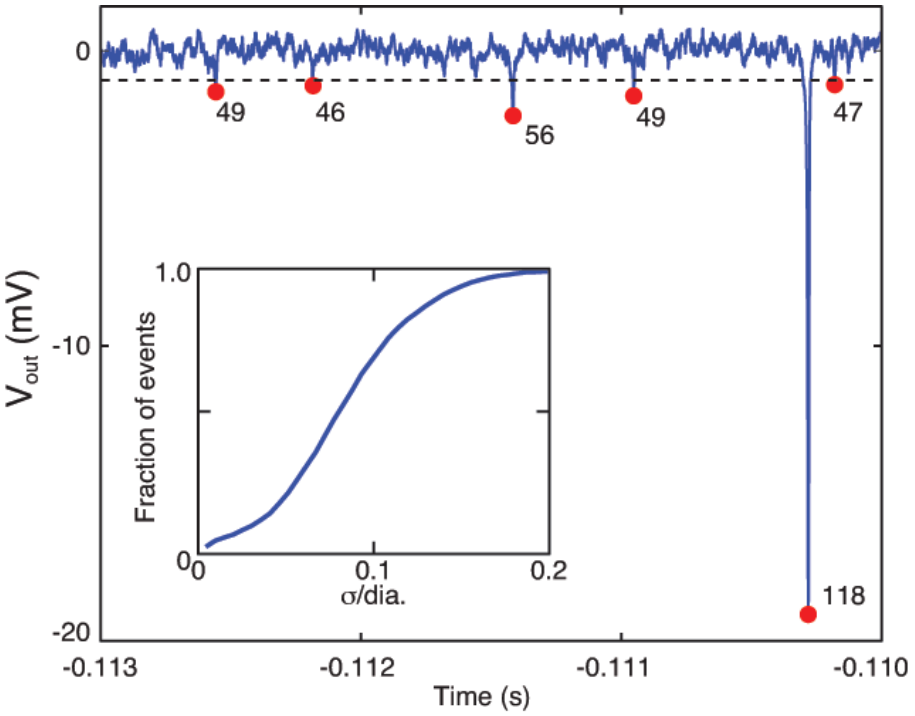

Supplementary Figure 3: Representative 3 ms subset of the voltage trace shown in Figure 6a showing detection of a single calibration particle and five smaller particles in the native plasma. Each peak is marked by a red circle, with adjacent number indicating the effective diameter (nm) after measurement of the peak amplitude (see Supplementary Notes). Inset shows the cumulative distribution of fractional uncertainty in measured peak diameters for the entire trace shown in Figure 6a. More than 70 % of peaks have uncertainty in their measured diameter that is less than 10%.

DOI: 10.1038/NNANO.2011.24

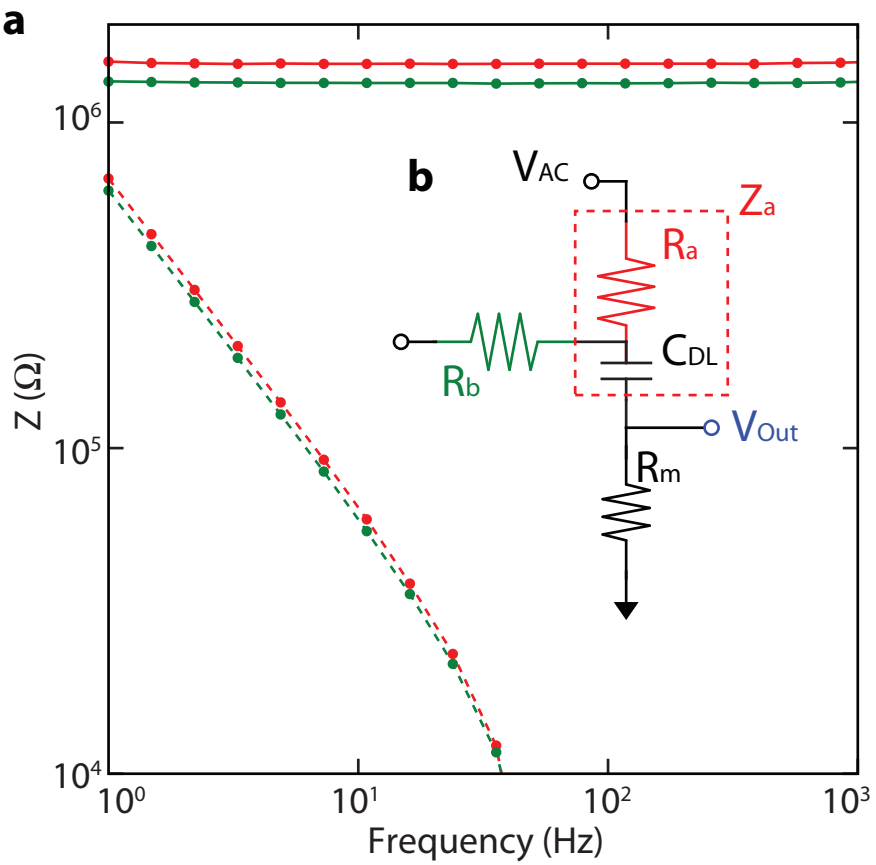

Supplementary Figure 4: Electrical characterization. Main panel: Measured electrical impedances Z_{a} (red) and Z_{b} (green) of the fluid paths between electrode pairs SH and SL respectively. Real and complex parts are plotted with solid and dashed lines respectively. The impedances Z_{a} and Z_{b} are each well-approximated by the series combination of resistor R_{a} or R_{b} respectively, and a common capacitor. The resistances are determined by the geometries of the fluid paths, and the capacitance is that of the electric double layer on the surface of the sensing electrode. Inset: Measurement configuration for the measurement of Z_{a}, modeled by the elements in red dashed outline.

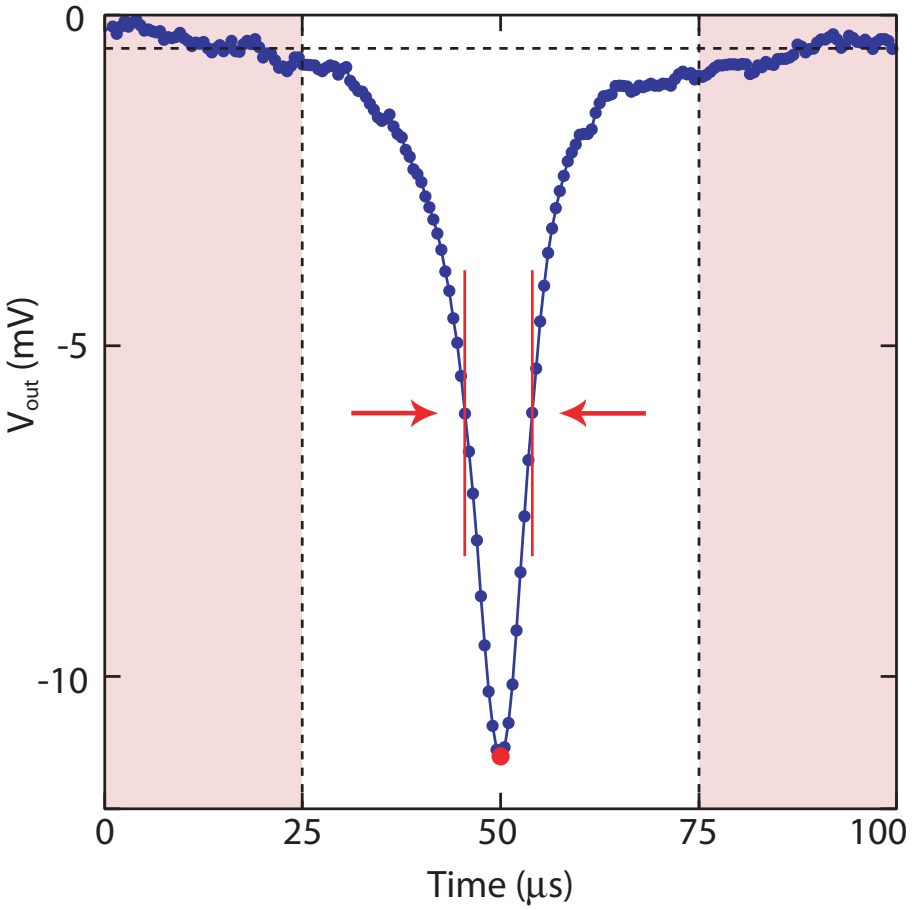

Supplementary Figure 5: Analysis window for a single 117 nm particle event. The amplitude of each peak in V_{out} was measured relative to the mean value of a local baseline (shaded outer regions). The peak width was measured at half-maximum relative to the mean local baseline, at the points indicated by the arrows.

DOI: 10.1038/NNANO.2011.24

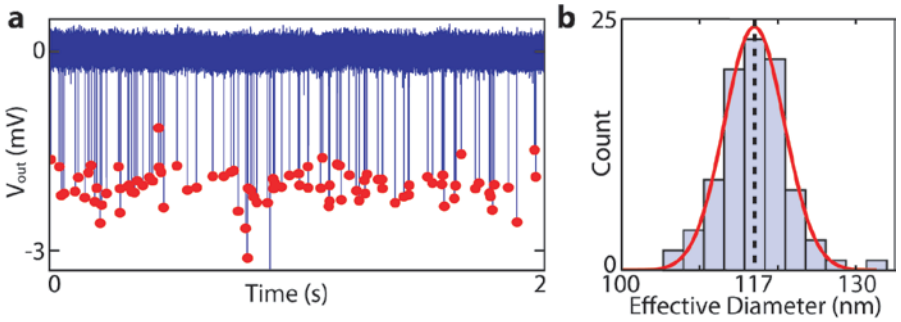

Supplementary Figure 6: Precision and detection bandwidth. (a) Representative two-second time trace of V_{out} showing detection of 92 distinct particles of mean diameter 117 nm, each particle marked by a red circle. The histogram of effective diameters calculated from these data is shown in (b), and displays smaller variance than the distribution of particle sizes specified by the manufacturer, demonstrating the precision of the sensor.

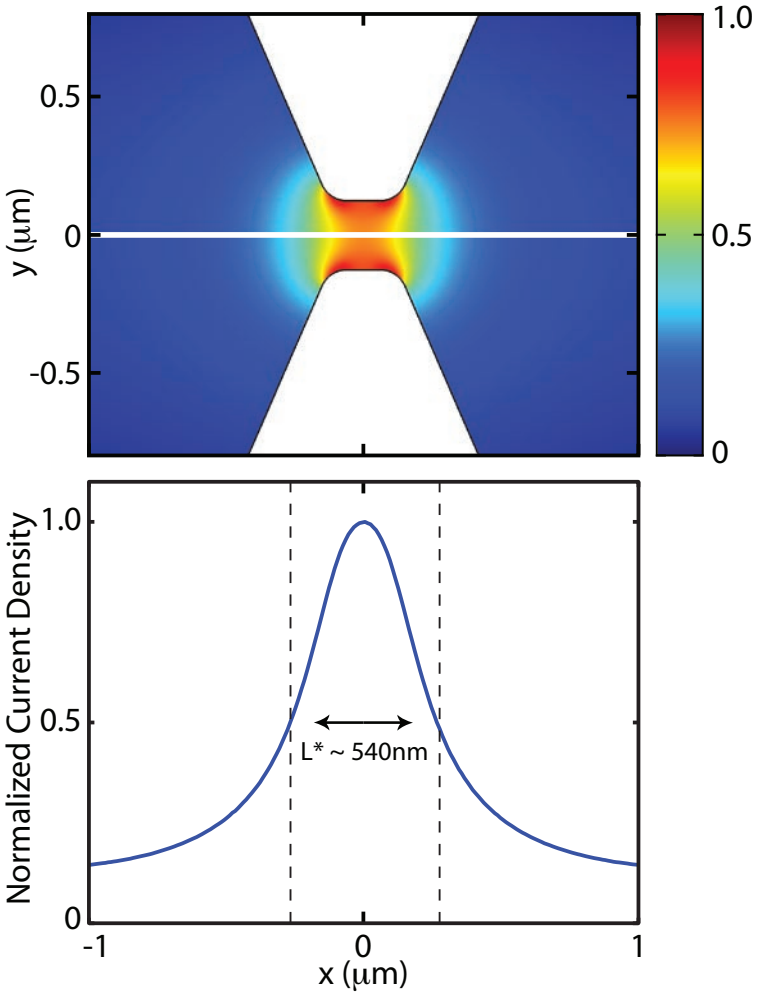

Supplementary Figure 7: Surface plot of the normalized current density in the region surrounding the nanoconstriction, with normalized cross-section values along the white line. The region of high current density as measured by peak width at half max along the cross section has length $L^{\star} \sim 540$ nm.

DOI: 10.1038/NNANO.2011.24

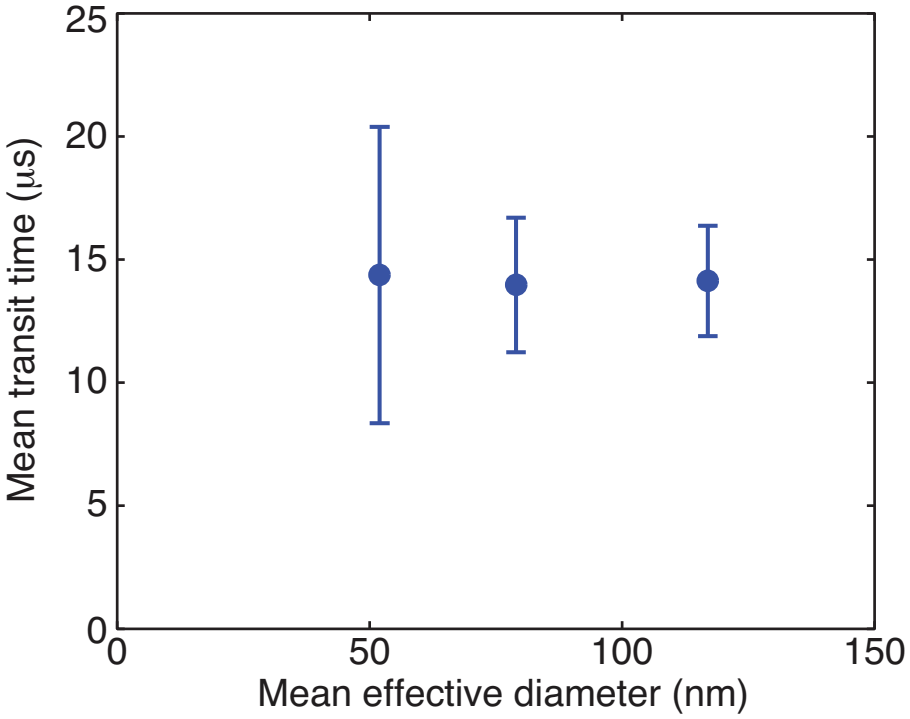

Supplementary Figure 8: Mean transit time plotted *vs* mean effective diameter for each of the populations in the mixture sampled in Figure 4. The mean transit times are 14 ± 6 μs, 14 ± 3 μs, and 14 ± 2 μs for the 50 nm, 75 nm and 117 nm particles respectively. Uncertainties are standard deviations in each mean.

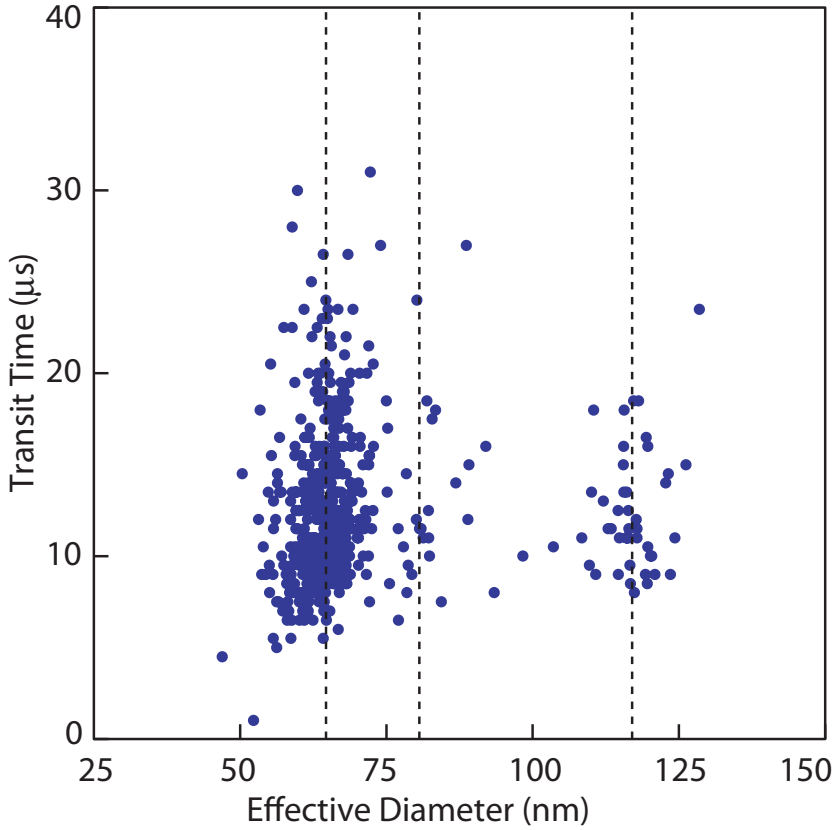

Supplementary Figure 9: Scatter plot of the measured transit times and diameters of particles detected in the mixture of T7 phage and 117 nm particles. The three groups with similar effective diameters (vertical bands) correspond to the phage (65 nm), phage dimers (81 nm) and 117 nm particles. The similar transit time distributions of the 65 nm and 81 nm groups suggests that the 81 nm group consisted of agglomerated pairs of phage virions (dimers), rather than coincidental passage of two individual phage virions.

References

[1] Bard, A. J. *Electrochemical Methods Fundamentals and Applications* (Wiley, 1980), second edn.

[2] DeBlois, R. W., Bean, C. P. & Wesley, R. K. A. Electrokinetic measurements with submicron particles and pores by the resistive pulse technique. *J. Colloid Interf. Sci.* **61**, 323–335 (1977).

[3] Uram, J. D., Ke, K., Hunt, A. J. & Mayer, M. Submicrometer pore-based characterization and quantification of antibody-virus interactions. *Small* **2**, 967–972 (2006).

DOI: 10.1038/NNANO.2011.24

[4] Saleh, O. A. & Sohn, L. L. An artificial nanopore for molecular sensing. *Nano Lett.* **3**, 37–38 (2003).

[5] Kubitscheck, H. E. *Counting and Sizing Micro-organisms with the Coulter Counter*, vol. 1, chap. XXVII, 593–610 (Academic Press, 1969).